

Fast, precise and shape-flexible registration of wavefronts

NIKOLAUS BERLAKOVICH^{1*}, ERNST CSENSICS¹, MARTIN FUERST¹, AND GEORG SCHITTER¹

¹Christian Doppler Laboratory for Precision Engineering for Automated In-Line Metrology, Automation and Control Institute (ACIN), TU Wien, 1040 Vienna, Austria

*Corresponding author: berlakovich@acin.tuwien.ac.at

Compiled August 11, 2021

In this paper, a fast and precise algorithm for wavefront reconstruction by the registration of wavefront segments is presented. If the wavefront exceeds the sensor aperture or the dynamic range of the sensor, a Shack-Hartmann sensor can measure only segments of an optical wavefront. The algorithm registers the wavefront segments in parallel, where they are simultaneously transformed to minimize their overlap mismatch for a precise reconstruction of the entire wavefront. The original nonlinear optimization problem is approximated by a convex optimization problem that can be solved more efficiently. A simulation-based analysis of the algorithm and a comparison to a previously proposed parallel registration (PR) as well as to the iterative closest point (ICP) algorithm is presented. It is shown that despite measurement noise the algorithm can precisely register plane as well as divergent wavefronts with root-mean-square registration errors smaller than 10 nm. Particularly for the divergent wavefront, this enables a reduction of the registration error by a factor of up to 750 as compared to the established algorithms. Analysis and comparison to the ICP and PR algorithm also show that the computation time of the proposed algorithm can be from one up to three orders of magnitude smaller. © 2021 Optical Society of America

OCIS codes: (150.1135) Algorithms; (120.3940) Metrology; (120.5050) Phase measurement; (220.4840) Testing; (280.4788) Optical sensing and sensors.

<http://dx.doi.org/10.1364/ao.XX.XXXXXX>

1. INTRODUCTION

A Shack-Hartmann sensor (SHS) is a device for the measurement of optical wavefronts and widely used in adaptive optics [1] and for the assessment of optical systems in ophthalmology [2], optical system alignment [3] and the production of optical systems and components [4]. The sensor is compact, insensitive to vibrations and provides a reference free measurement with significant dynamic range [4, 5]. However, wavefronts larger than the sensor aperture or wavefronts containing huge aberrations beyond the dynamic range of the sensor can not be directly measured by the SHS. Typically, such wavefronts are transformed into measurable wavefronts by additional optics, e.g. null optics. But supporting optics cause additional aberrations in the resulting wavefront and their application is limited to the respective wavefront shape [6, 7]. In [8–10] a measurement concept without these drawbacks is proposed. The SHS measures parts of the wavefront, i.e. wavefront segments at different locations, where the entire set of measured wavefront segments contains the entire information of the wavefront. In case of overlapping measurements the entire wavefront can be reconstructed from the set of wavefront

segments by registration algorithms. To enable a qualitative evaluation of the optical system by the registered wavefront, small registration errors are crucial. Apart from that, the computation time of the registration process is a relevant quantity, especially in industrial cases like inline metrology [11], where measurement times on the subsecond scale are demanded. Besides conventional spherical lenses, lenses with arbitrary surface shapes, i.e. freeform optics, grow in popularity as they provide high quality optical performance and compactness of the optical system [12]. As the wavefront shape of freeform optics may vary significantly, ranging from plane to highly divergent shapes, there is the need for a registration algorithm capable of registering plane as well as divergent wavefronts. Recently, an accurate registration algorithm robust to measurement noise and based on parallel subpixel registration was proposed [13]. The algorithm registers the wavefront segments by minimizing a nonlinear mismatch metric, which might take a computation time too large for specific applications. Moreover, analysis shows that the registration performance of the algorithm decreases with respect to increasingly divergent wavefronts.

The contribution of this paper is the development and evaluation of a parallel registration algorithm that enables fast, precise and wavefront-shape-flexible registration. Section 2 introduces the algorithm and discusses its properties. Section 3 presents a simulative analysis of the algorithm and Section 4 concludes the paper.

2. ALGORITHM DESCRIPTION

A. Measurement concept

In [9] a measurement concept is proposed, where the SHS is moved along a scan trajectory and measures parts of the wavefront, i.e. wavefront segments, at specific sensor positions. The sensor aperture at a specific sensor position is called a subaperture. For the reconstruction of the entire wavefront the sensor position and alignment at each measurement position is essential. However, due to uncertainties and errors in the positioning system, the actual measurement positions deviate from the nominal measurement positions (see Fig. 1). Hence, to obtain the entire wavefront, the wavefront segments have to be registered via rigid body transformation and wavefront propagation (see Fig. 2). Wavefront propagation is necessary to compensate for the phase difference between wavefront segments, as the scan trajectory might deviate from the wavefront of a specific phase as illustrated in Fig. 1.

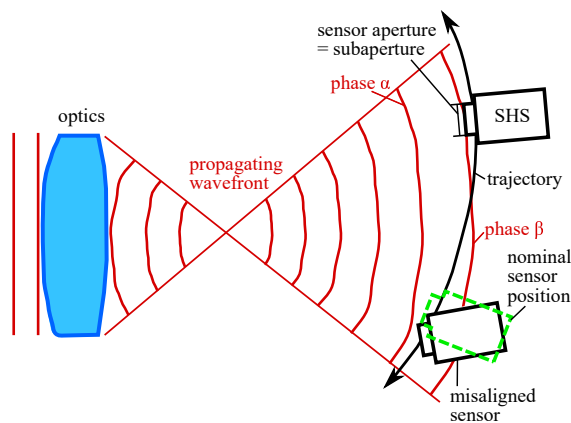


Fig. 1. Measurement concept, where the wavefront is measured at different SHS positions. The actual sensor position is typically subject to the uncertainty of the positioning system. The scan trajectory may traverse an entire phase interval causing phase differences between the measured wavefront segments.

Before the registration of the wavefront segments, the segments have to be reconstructed from the corresponding SHS measurements. At each lenslet of the SHS the average gradient over the lenslet area of the wavefront that intersects with the lenslet is measured. The local gradient of the wavefront at the center of the lenslet is typically well approximated by the measured average gradient [14]. Most likely the wavefronts intersecting with different lenslets are not belonging to the same phase, meaning that each gradient measurement corresponds to a different phase value. For plane wavefronts the differences between the phase values of the gradient measurements are small and all gradients can be interpreted as the gradients of

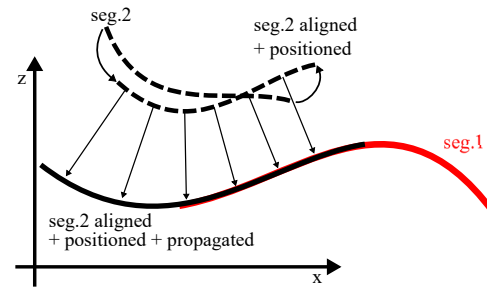


Fig. 2. For registration the wavefront segments are aligned, positioned and propagated. Alignment and positioning are equal to a rigid body transformation.

one wavefront, i.e. one phase. However, in the case of strongly aberrated wavefronts this assumption is not valid, as the differences between the phase values of the gradient measurements are no longer small (see Fig. 3a). In this case the phase values of the gradient measurements have to be reconstructed, as a direct wavefront reconstruction from the gradients is not possible. Thus also the phase gradient is determined [15], next to the wavefront gradient itself, which enables the computation of the phase value at the center of each lenslet. As for the wavefront, the phase values can be derived from the phase gradients by a zonal or modal reconstruction algorithm [16, 17]. In particular, the calculated phase values are differences between the absolute phase values and the absolute phase value of a reference wavefront, due to the fact that absolute phase values cannot be measured with a SHS, as illustrated in Fig. 3a. The point cloud of a wavefront with specific phase is then determined by propagating each wavefront point that intersects a lenslet center with the corresponding negative phase value, as illustrated in Fig. 3b.

For the reconstruction of the wavefront or the phase distribution a zonal reconstruction is preferred, as it better preserves details of the wavefront [18].

Besides the point cloud, the normal vectors of the wavefront segment at the points of the point cloud are determined, as they are directly derived from the direction of back-propagation.

B. Fast registration of two wavefront segments

The point cloud of segment i positioned in the global frame (FG) based on the corresponding nominal sensor position is denoted by P_{0i} . After wavefront segment reconstruction, P_{0i} is represented in the coordinate system FSi, i.e. P_{0i}^i with elements $x_{0ij}^i \in \mathbb{R}^3$ and the corresponding normal vectors $n_{0ij}^i \in \mathbb{R}^3$. The upper index defines the coordinate system in which the objects are represented and j is an index for numeration of the points. FSi denotes the coordinate system of subaperture i with nominal measurement position, where the x - y plane of the system lies in the plane of the subaperture. Hence, points represented in FSi are transformed to FG by a rigid body transformation in terms of parameters $\psi_i, v_i \in \mathbb{R}^3$, which denote the nominal sensor alignment and position. In Fig. 4 the defined coordinate systems and point clouds are illustrated. For subpixel registration P_{0i}^i and the corresponding normal vectors are interpolated. $F_i(x, y) \in \mathbb{R}$ is the interpolant of the points x_{0ij}^i and $N_i(x, y) \in \mathbb{R}^3$ the one of the normal vectors n_{0ij}^i in terms of the x - y coordinates of FSi. $N_{ik}(x, y) \in N_i(x, y)$ denotes the interpolant of one component

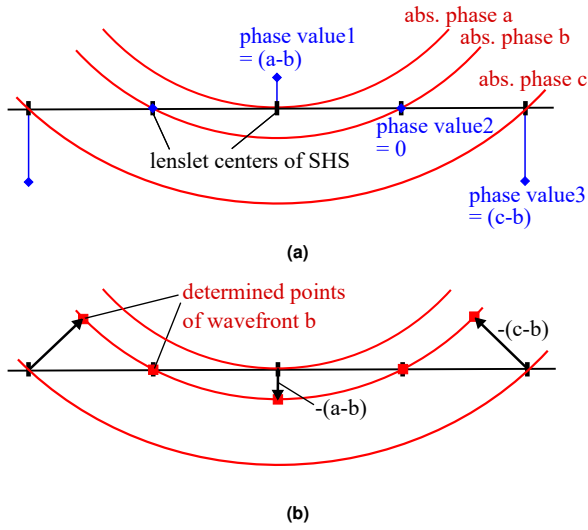


Fig. 3. Wavefronts of different phases intersect with the lenslets of the SHS. The phase value at the center of each lenslet relative to a reference phase is determined from the measured phase gradients (a). The point cloud of a wavefront is determined by back-propagating each wavefront point intersecting a lenslet center with the negative phase value (b).

of the normal vectors. To enable registration, P_{0i}^i is transformed by rigid body transformation and wavefront propagation and the transformed points and normal vectors are

$$\begin{aligned} \mathbf{x}_{ij}^i(\mathbf{a}_i) &= \mathfrak{R}(\theta_i) (\mathbf{x}_{0ij}^i + s_i \mathbf{n}_{0ij}^i) + \mathbf{k}_i \in P_i^i(\mathbf{a}_i) \quad \text{and} \\ \mathbf{n}_{ij}^i(\mathbf{a}_i) &= \mathfrak{R}(\theta_i) \mathbf{n}_{0ij}^i, \end{aligned} \quad (1)$$

where $\mathfrak{R}(\theta_i)$ is a matrix describing the rotation in terms of $\theta_i \in \mathbb{R}^3$, $\mathbf{k}_i \in \mathbb{R}^3$ is the translation vector and $s_i \in \mathbb{R}$ denotes the propagation distance. The parameters are collected in the vector $\mathbf{a}_i^T = (\mathbf{k}_i^T, \theta_i^T, s_i) \in \mathbb{R}^7$ (see Fig. 4). The registration of two wavefront segments ($i = 1, 2$) can be carried out by minimizing the metric

$$\mathfrak{M}_{12}(\mathbf{a}_1, \mathbf{a}_2) = \sum_n (W_2^1(q_{21n}, \mathbf{a}_2) - W_1^1(q_{21n}, \mathbf{a}_1))^2, \quad (2)$$

where $W_1^1(\cdot, \mathbf{a}_1) = W_1^1(\mathbf{a}_1)$ and $W_2^1(\cdot, \mathbf{a}_2) = W_2^1(\mathbf{a}_2)$ are functions describing the transformed segments respectively in the FS1 coordinate system. $q_{21n} \in \mathbb{R}^2$ denotes a sampling point in the x - y plane of FS1 belonging to the overlapping region of the segments. The difference between the functions is squared to register the segments in the least squares sense. The segment functions contain the corresponding point clouds described by Eq. 1 (see Fig. 5), i.e.

$$\begin{aligned} \mathbf{x}_{1j}^1(\mathbf{a}_1) &\in P_1^1(\mathbf{a}_1) \subset W_1^1(\mathbf{a}_1), \\ \mathbf{x}_{2j}^1(\mathbf{a}_2) &= \mathfrak{R}^{2 \rightarrow 1} \mathbf{x}_{2j}^2(\mathbf{a}_2) + \mathfrak{T}^{2 \rightarrow 1} \in P_2^1(\mathbf{a}_2) \subset W_2^1(\mathbf{a}_2) \quad \text{with} \quad (3) \\ \mathbf{n}_{2j}^1(\mathbf{a}_2) &= \mathfrak{R}^{2 \rightarrow 1} \mathbf{n}_{2j}^2(\mathbf{a}_2), \end{aligned}$$

where $\mathfrak{R}^{2 \rightarrow 1}$ and $\mathfrak{T}^{2 \rightarrow 1}$ are rotation matrix and translation vector in terms of $\psi_1, \psi_2, \mathbf{v}_1, \mathbf{v}_2 \in \mathbb{R}^3$ to transform objects from FS2 to FS1. $\chi_n^1 \in P_{02}^1 = P_2^1(\mathbf{a}_2 = 0)$ are those points that overlap with

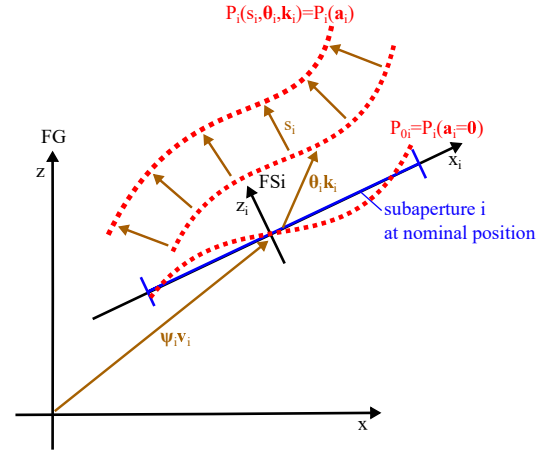


Fig. 4. Defined point clouds and coordinate systems. P_{0i} defines the point cloud of segment i at the nominal subaperture position in FG. P_{0i} is rigid body transformed by $\{\mathbf{k}_i, \theta_i\}$ and propagated by the distance s_i resulting in the point cloud $P_i(\mathbf{a}_i) = P_i(\mathbf{k}_i, \theta_i, s_i)$. The point clouds represented in FSi are denoted by P_{0i}^i and $P_i^i(\mathbf{a}_i)$.

$W_1^1(\mathbf{a}_1 = 0)$ and the corresponding normal vectors are denoted by η_n^1 . The x and y component of $\chi_n^1 \in \mathbb{R}^3$ define the sampling points

$$q_{21n}^T = (\chi_{n1}^1, \chi_{n2}^1). \quad (4)$$

With Eq. 4 χ_n^1 and η_n^1 are point and normal vector of $W_2^1(\mathbf{a}_2 = 0)$ at q_{21n} , as illustrated in Fig. 5. As $W_1^1(\mathbf{a}_1 = 0)$ contains $P_{01}^1 = P_1^1(\mathbf{a}_1 = 0)$, it is equal to F_1 . Hence, point and normal vector of $W_1^1(\mathbf{a}_1 = 0)$ at q_{21n} are given by

$$\begin{aligned} \tilde{\chi}_n^1 &= (\chi_{n1}^1, \chi_{n2}^1, F_1(q_{21n})), \\ \tilde{\eta}_n^1 &= N_1(q_{21n}), \end{aligned} \quad (5)$$

where N_1 is the interpolant of the normal vectors corresponding to P_{01}^1 .

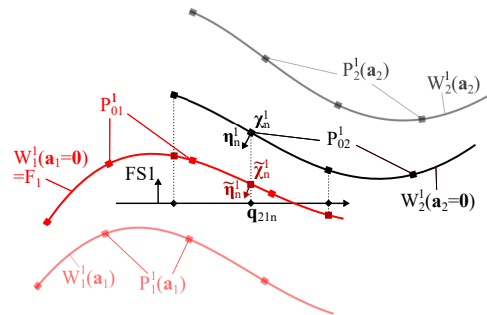


Fig. 5. Segment functions in terms of transformation parameters in FS1. $W_1^1(\mathbf{a}_1)$ and $W_2^1(\mathbf{a}_2)$ contain the point clouds $P_1^1(\mathbf{a}_1)$ and $P_2^1(\mathbf{a}_2)$. $\chi_n^1 \in P_{02}^1$ and η_n^1 denote the point and normal vector of $W_2^1(\mathbf{a}_2 = 0)$ at the sampling point q_{21n} . Point and normal vector of $W_1^1(\mathbf{a}_1 = 0)$ at q_{21n} are $\tilde{\chi}_n^1$ and $\tilde{\eta}_n^1$ determined by Eq. 5.

If \mathbf{a}_1 and \mathbf{a}_2 are sufficiently small, the segment functions can be approximated around q_{21n} by functions with linear dependences on $\mathbf{a}_1^T = (\mathbf{k}_1^T, \theta_1^T, s_1)$ and $\mathbf{a}_2^T = (\mathbf{k}_2^T, \theta_2^T, s_2)$ given by

$$\begin{aligned} W_2^1(q_{21n}, \mathbf{a}_2) &= \chi_{n3}^1 + \frac{1}{\eta_{n3}^1} [\eta_{n3}^{2T} \mathbf{k}_2 + \sum_{v=1}^3 \eta_{n3}^{2T} \eta_{nv}^1 \chi_n^2 \theta_{2v} + s_2] \\ &= \chi_{n3}^1 + \mathbf{C}_{12n}^T \mathbf{a}_2, \\ W_1^1(q_{21n}, \mathbf{a}_1) &= \tilde{\chi}_{n3}^1 + \frac{1}{\tilde{\eta}_{n3}^1} [\tilde{\eta}_{n3}^{1T} \mathbf{k}_1 + \sum_{v=1}^3 \tilde{\eta}_{n3}^{1T} \eta_{nv}^1 \tilde{\chi}_n^1 \theta_{1v} + s_1] \\ &= \tilde{\chi}_{n3}^1 + \tilde{\mathbf{C}}_{12n}^T \mathbf{a}_1, \end{aligned} \quad (6)$$

where $\eta_{nv}^1 = \frac{d\eta_n(\theta)}{d\theta_v} \big|_{\theta=0}$ with $\eta(\theta)$ the rotation matrix in Eq. 1 and $\mathbf{C}_{12n}, \tilde{\mathbf{C}}_{12n} \in \mathbb{R}^7$ are vectors including the coefficients of \mathbf{a}_2 and \mathbf{a}_1 . $\chi_{n3}^1, \tilde{\chi}_{n3}^1, \eta_{n3}^1, \tilde{\eta}_{n3}^1$ denote the z components of $\chi_n^1, \tilde{\chi}_n^1, \eta_n^1, \tilde{\eta}_n^1$. \mathbf{C}_{12n} and $\tilde{\mathbf{C}}_{12n}$ can be determined with $\chi_n^2 \in P_{02}^2$, $\chi_n^1 \in P_{02}^1$ calculated by transforming χ_n^2 (see Eq. 3), $\tilde{\chi}_n^1$ determined by χ_n^1 together with the interpolant of P_{01}^1 (see Eq. 5) and the corresponding normal vectors. This makes Eq. 6 convenient, as the coefficients can be quickly determined with the point clouds and normal vectors that are available after the wavefront segment are reconstructed. Considering Eq. 6 the metric (see Eq. 2) can be written as

$$\begin{aligned} \mathfrak{M}_{12}(\mathbf{a}_1, \mathbf{a}_2) &= \sum_n (\chi_{n3}^1 + \mathbf{C}_{12n}^T \mathbf{a}_2 - \tilde{\chi}_{n3}^1 - \tilde{\mathbf{C}}_{12n}^T \mathbf{a}_1)^2 \\ &= \sum_n (\mathbf{C}_{12n}^T \mathbf{a}_2 - \tilde{\mathbf{C}}_{12n}^T \mathbf{a}_1 - B_{12n})^2, \end{aligned} \quad (7)$$

where $B_{12n} = \tilde{\chi}_{n3}^1 - \chi_{n3}^1 \in \mathbb{R}$. Equation 7 enables minimization of \mathfrak{M}_{12} by solving a system of linear equations.

In Eq. 6 the segment functions are approximated around the points χ_n^1 and $\tilde{\chi}_n^1$. Hence, registration based on this approximation is better the closer $\tilde{\chi}_n^1$ is to the correspondence of χ_n^1 in $W_1^1(\mathbf{a}_1 = 0)$. Typically, orthogonal projection provides a good estimation of the correspondence [19]. Considering Eq. 5, $\tilde{\chi}_n^1$ is determined by projection of χ_n^1 onto $W_1^1(\mathbf{a}_1 = 0)$ along the z -axis. Since the segments are represented in FS1, where the projection along the z -axis is a good approximation of the orthogonal projection (see Fig. 6) due to the limited dynamic range of a SHS and the typical scale of sensor misalignment [13], with Eq. 5 correspondences are well approximated. Therefore, with Eq. 7 the segments can be registered in FS1 independently of their orientation in FG, enabling the registration of highly divergent wavefronts.

C. Fast parallel registration of a set of wavefront segments

Equation 7 is an approximation of the overlap mismatch between two wavefront segments in terms of parameters related to rigid body transformation and wavefront propagation. The entire overlap mismatch of a set of wavefront segments $i = 1..U$, each transformed by parameters \mathbf{a}_i , is determined by the sum over all overlap mismatches of overlapping segment pairs. As each overlap mismatch of a segment pair can be approximated by Eq. 7, the entire overlap mismatch is approximated by

$$\begin{aligned} \mathfrak{M}_g(\mathbf{A}) &= \sum_{i,k} \mathfrak{M}_{ik}(\mathbf{a}_i, \mathbf{a}_k) \\ &= \sum_{i,k} \sum_n (\mathbf{C}_{ikn}^T \mathbf{a}_k - \tilde{\mathbf{C}}_{ikn}^T \mathbf{a}_i - B_{ikn})^2, \end{aligned} \quad (8)$$

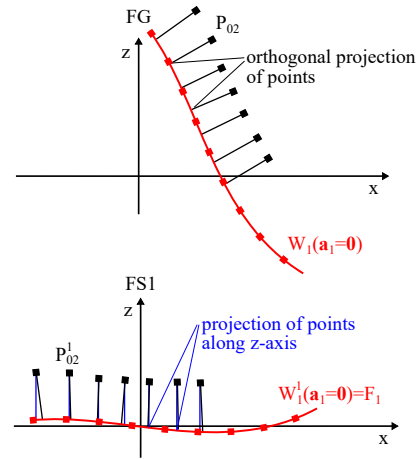


Fig. 6. In FS1 the projection of $\chi_n^1 \in P_{02}^1$ along the z -axis onto $W_1^1(\mathbf{a}_1 = 0)$ approximates the orthogonal projection.

where $\mathbf{A}^T = (\mathbf{a}_1^T, \dots, \mathbf{a}_U^T) \in \mathbb{R}^{7U}$. Minimization of Eq. 8 is a convex optimization problem and can be written as the matrix equation

$$\mathbf{Q}^T \mathbf{Q} \mathbf{A} = \mathbf{Q}^T \mathbf{B}, \quad (9)$$

where $\mathbf{Q} \in \mathbb{R}^{V \times 7U}$ and $\mathbf{B} \in \mathbb{R}^V$ with V denoting the total number of squared terms in Eq. 8. A term $(\mathbf{C}_{ikn}^T \mathbf{a}_k - \tilde{\mathbf{C}}_{ikn}^T \mathbf{a}_i - B_{ikn})^2$ is related to a row of \mathbf{Q} and \mathbf{B} given by $(k < i)$

$$\mathbf{Q} = \begin{pmatrix} & (k-1)7 & & k7+1 & & (i-1)7 & & i7+1 \\ & \vdots & & \vdots & & \vdots & & \vdots \\ 0 & \dots & 0 & \mathbf{C}_{ikn}^T & 0 & \dots & 0 & -\tilde{\mathbf{C}}_{ikn}^T & 0 & \dots & 0 \\ & \vdots & & \vdots & & \vdots & & \vdots \end{pmatrix} \quad (10)$$

and

$$\mathbf{B} = \begin{pmatrix} \vdots \\ B_{ikn} \\ \vdots \end{pmatrix}. \quad (11)$$

The matrix $\mathbf{Q}^T \mathbf{Q}$ is singular as by registration the entire wavefront is determined up to a rigid body transformation and a wavefront propagation denoted by seven transformation parameters. To solve Eq. 9 the seven transformation parameters ($\mathbf{a} \in \mathbb{R}^7$) of one wavefront segment are set to 0, which is conveniently the wavefront segment in the center of the set of segments to keep registration parameters small. Equation 9 can then be efficiently solved with the Cholesky decomposition [20]. To enable subpixel registration the point cloud and normal vectors of one segment of each overlapping pair in Eq. 8 are interpolated. For the sake of efficiency it is convenient to use the interpolants of one segment for as many overlaps as possible. For the registration of plane wavefronts the arrangement of interpolated segments and not interpolated segments in a

chessboard pattern is proposed [13] if the primary overlaps between the segments are considered.

The proposed registration algorithm enables fast parallel registration (FPR) of the wavefront segments and can be summarized in three steps. First, the point clouds and normal vectors of a subset of segments are interpolated so that each overlapping pair contains one interpolated segment. Second, correspondences are determined with the interpolants (see Eq. 5). Third, the matrix Q and the vector B are constructed with quantities of Eq. 6 and registration is carried out by solving Eq. 9.

3. ALGORITHM ANALYSIS

The registration performance of the FPR algorithm is analysed via simulations with respect to sensor misalignment, measurement noise, etc. and compared to the performance of the parallel registration (PR) algorithm [13] and the point-to-plane iterative closest point (ICP) algorithm [21]. With the ICP algorithm the wavefront segments are sequentially registered, which means that registration is carried out in several individual registration processes, where in each registration process one wavefront segment is added to the registered wavefront using the ICP algorithm.

A. Simulation setting

In the scope of this analysis two sets of simulated wavefronts are considered. One is a plane wavefront with a diameter of 50 mm containing aberrations with a peak to valley of 11 μm , which results from the collimation of a spherical wavefront with a meniscus lens [13, 22]. The other one is a spherical wavefront with a diameter of 30 mm and a divergence of 140°. Due to the propagation through a cover slip with 170 μm thickness, the divergent wavefront contains aberrations with a peak to valley of 5 μm . With the software OpticStudio (Zemax LLC, Kirkland, WA, USA) both wavefronts are obtained by ray tracing simulations. The plane wavefront is measured at 5x5 square subapertures, each with a side length of 13 mm, as illustrated in Fig. 7a. The divergent wavefront is measured at 43 circular subapertures with a respective diameter of 7 mm, as depicted in Fig. 7b. Owing to the symmetry of a sphere, the dynamic range of the SHS limits the size of the subaperture to a circle, as the dynamic range is reached at a specific radius on the sensor aperture. The measurement is simulated using a MATLAB (The MathWorks Inc., Natick, MA, USA) based software, which can also consider sensor misalignment and measurement noise. The dimensions of the subapertures are on the order of the dimension of a sensor aperture of a state of the art SHS [23]. Similarly, the dimensions of the simulated lenslets of $130 \times 130 \mu\text{m}^2$ are set to realistic values. The lenslets are arranged in a rectangular grid, leading to 10.000 lenslets per subaperture for the plane wavefront and about 2.200 lenslets per subaperture for the divergent wavefront. The wavefront segments are reconstructed with a spline-based zonal reconstruction algorithm [24] which reconstructs the segments of both wavefronts with a root mean square (RMS) reconstruction error of at most 0.1 nm. The segments are then registered by the algorithms. The interpolation of point clouds of the segments is based on cubic interpolation, as with cubic interpolation the RMS interpolation error of the wavefronts is smaller 0.1 nm while being up to 100 nm with linear interpolation especially for the divergent wavefront. Interpolation of the normal vectors is based on linear interpolation, as the normal vector is typically a function of less order than

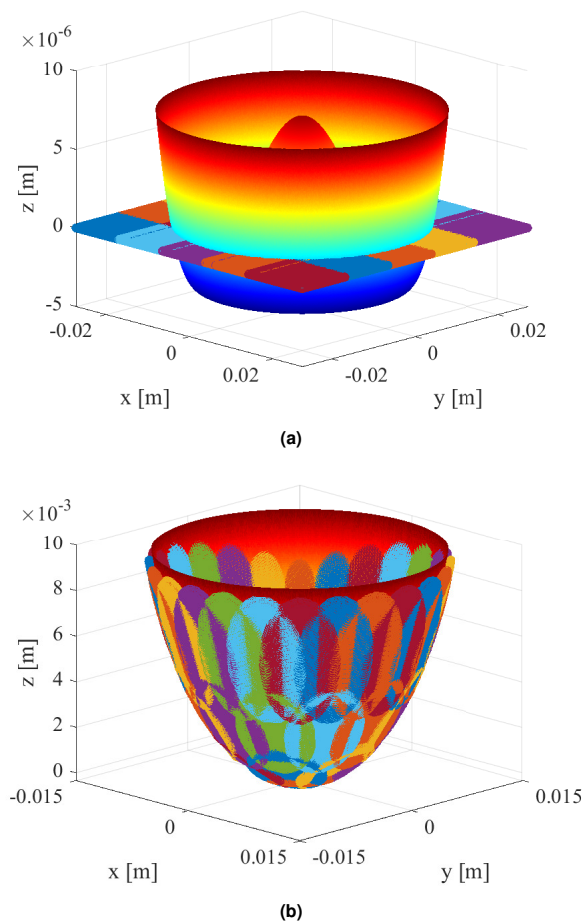


Fig. 7. Plane wavefront (PV=11 μm) virtually measured at 25 square subapertures (a) and divergent wavefront (PV=5 μm) with 140° divergence virtually measured at 43 circular subapertures (b).

the wavefront. Moreover, the interpolation error of the normal vector is less critical, as it causes an error of second order in a propagated wavefront. For the ICP algorithm, the wavefront segment in the center of the set of wavefront segments is set to the initial segment. The other segments are then sequentially added in a spiral way [13].

For evaluation of the reconstruction first, the registered wavefront is fitted into the exact wavefront and the difference between the wavefronts is calculated. Second, the registration errors are determined by removing the noise components from the difference. Third, the RMS and peak to valley (PV) of the registration errors are computed for comparison of the various algorithm results.

B. Reference configuration

Considering Eq. 1, θ_i reflects rotational misalignment and k_i translational misalignment of a wavefront segment. Misalignment is simulated by randomly distributed components of θ_i and k_i between $[-100, 100] \mu\text{rad}$ and $[-1, 1] \mu\text{m}$ respectively.

The simulated measurement noise has zero mean, a standard deviation of 10 nm and is contained in the point clouds as well as the normal vectors [13]. The overlap area between subapertures is 20 % of the subaperture area. Considering the divergent wavefront (see Fig. 7b), the overlap size of the wavefront is at least 20 % of the subaperture area or larger, owing to the complex wavefront shape. For each wavefront segment pair only points belonging to the overlap area can be used for registration. The number of points per overlap (PPO) used for registration is set to its maximum value, i.e. all points belonging to the overlap are used leading to an average of 928 PPO for the plane wavefront and 315 PPO for the divergent wavefront.

The plane wavefront and the divergent wavefront are registered by the algorithms, with the resulting registration errors for the FPR, PR and ICP algorithm depicted in Fig. 8 and Fig. 9. Considering the divergent wavefront the FPR algorithm gives a result that is two orders of magnitude better than those of the other algorithms. While the RMS registration error of the FPR algorithm is 9 nm those of the PR and ICP algorithm are 640 nm and 5 μ m. The decrease of registration performance of the PR algorithm is explained by the fact that the PR algorithm minimizes the original global mismatch metric, which contains local minima. The extent of the local minima depends on the shape and errors in the wavefront segments, e.g. due to measurement noise. As wavefront propagation and translation along the z-axis have similar effects on a segment, the PR algorithm typically gets caught into local minima with respect to these parameters. While the remaining phase difference between the wavefront segments has less impact to registration errors for plane wavefronts, it might lead to large registration errors for divergent wavefronts. The FPR algorithm can not get caught into a local minimum as the approximation of the global mismatch metric (see Eq. 8) is a convex function that contains no local minimum but one global minimum. As long as the approximation is good, the global minimum of Eq. 8 is close to the global minimum of the original global mismatch metric and the FPR algorithm shows accurate results. Moreover, the FPR algorithm shows slightly larger registration errors for the divergent wavefront as compared to the plane wavefront. The increased registration errors can be explained by the fact that for the divergent wavefront first, a smaller number of PPO is available and second, a larger number of wavefront segments is registered.

There are two reasons for the large registration errors of the ICP algorithm concerning the divergent wavefront. First, the ICP algorithm can not propagate the wavefront segments and the initial phase difference between the wavefront segments remains, leading to large registration errors concerning divergent wavefronts. Second, due to sequential registration the registration errors accumulate much stronger than in parallel registration and the impact of phase difference is increased, leading to huge registration errors and cracks in the registered wavefront (see Fig. 9c).

The registration with the algorithms is carried out on a personal computer with 6 cores and a processor frequency of 2.6 GHz. While the PR algorithm needs around 100 s to 200 s and the ICP algorithm around 2 s to register the wavefront segments, the FPR algorithm requires only about 100 ms, suggesting its applicability for real-time applications.

The simulation configuration of this section is the reference configuration for the subsequent sections, where in each section the algorithms are analysed with respect to one of the quantities sensor misalignment, measurement noise, number of points per overlap used for registration and the percentage of overlap

with respect to the subaperture area. Only the quantity under consideration is altered, while the other quantities remain at the reference configuration value.

C. Influence of misalignment

The sensor misalignment at a specific measurement position can be divided into rotational and translational misalignment, described by θ_i and k_i (see Eq. 1). The two types of misalignment are simulated by a random choice of the corresponding parameters within predefined misalignment ranges, i.e. $\pm r_\theta$ and $\pm r_k$. The RMS registration errors of the algorithms considering both wavefronts and different misalignment ranges are shown in Table 1. Besides results for combined types of misalignment, results for low translational misalignment ranges as well as low rotational misalignment ranges are depicted. The PV error is typically a factor 5 to 8 larger than the RMS error. Concerning the plane wavefront, the FPR algorithm shows a slightly better robustness to sensor misalignment than the other algorithms. Concerning the divergent wavefront, the FPR algorithm has registration errors a factor 75 smaller than the PR algorithm and at least a factor around 750 smaller than the ICP algorithm.

The reason for the registration errors of the PR algorithm are local minima in the global mismatch metric. Typically a phase difference remains, causing registration errors in divergent wavefronts. The convergence into the global minimum depends on the initial configuration of the wavefront segments. Hence, the PR algorithm gets caught into a different local minimum by a change of misalignment, which explains the strong variations of the registration errors of the PR algorithm considering the divergent wavefront.

The large registration errors of the ICP algorithm are explained by the accumulation of registration errors and its incapability to compensate phase differences between wavefront segments. Moreover concerning the divergent wavefront, results show a strong variation of the registration errors of the ICP algorithm with a change of misalignment. In the FPR algorithm the global mismatch metric is approximated with a convex function including no local minima that compromise the registration performance.

Table 1. RMS registration error in dependence of misalignment ranges for FPR, PR and ICP algorithm with respect to the plane and the divergent wavefront.

r_θ	r_k	FPR	PR	ICP	FPR	PR	ICP
(μ rad)	(μ m)	plane	plane	plane	div.	div.	div.
		(nm)	(nm)	(nm)	(nm)	(nm)	(nm)
100	1	4	3	7	9	640	5000
100	0.5	4	5	7	8	600	10000
200	0.5	4	4	7	8	600	3000
15	1	4	8	7	8	150	15000
15	5	5	7	6	10	900	6000
200	5	5	12	7	9	1000	15000

D. Influence of noise

The measurement noise of a SHS can have several sources, e.g. background light, readout and dark current [25]. Figure 10

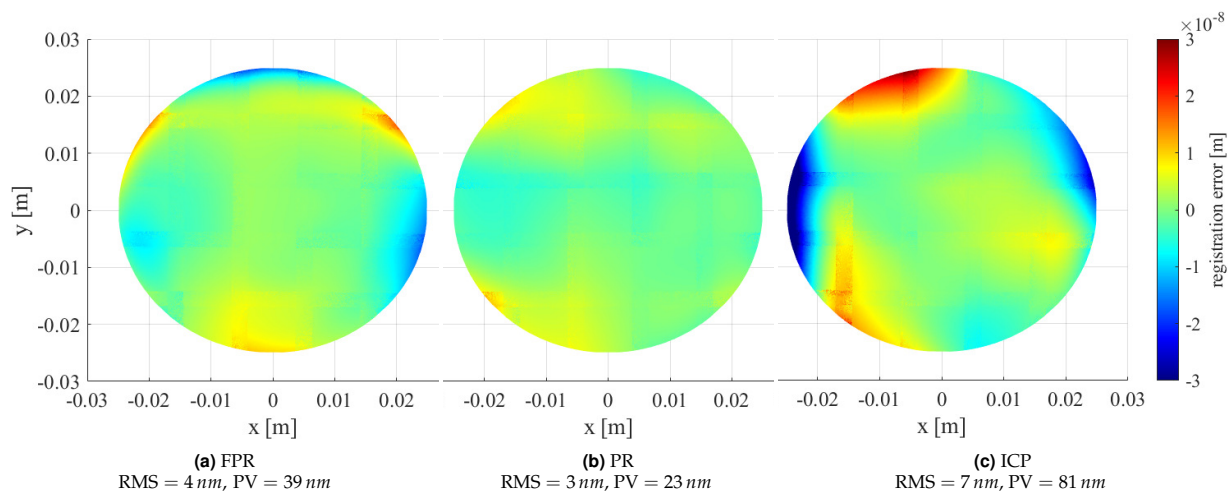


Fig. 8. Registration error of the reconstructed plane wavefront of the FPR (a), PR (b) and ICP (c) algorithm with respect to the exact wavefront.

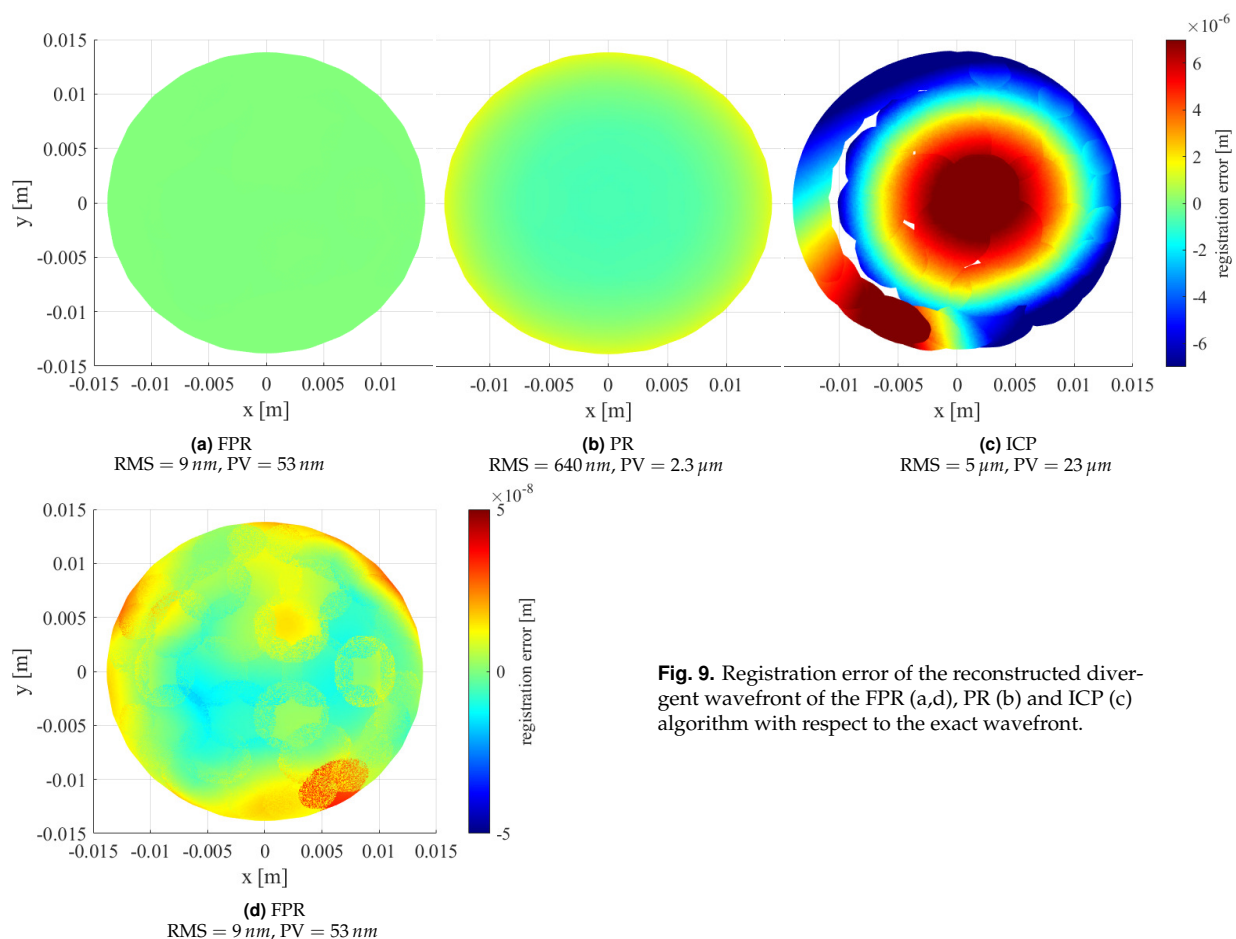


Fig. 9. Registration error of the reconstructed divergent wavefront of the FPR (a,d), PR (b) and ICP (c) algorithm with respect to the exact wavefront.

shows the RMS registration error of the algorithms in depen-

dence of the standard deviation of noise for both wavefronts.

The algorithms show comparable robustness to measurement noise concerning the plane wavefront. However, considering the divergent wavefront the PR algorithm shows large registration errors, while the FPR algorithm still shows accurate registration results. The ICP algorithm shows less robustness to measurement noise as registration errors accumulate due to sequential registration. For the divergent wavefront the registration error of the ICP algorithm shows in general large values and also large variations with even decreasing errors for increased noise standard deviation levels. This is explained, as the noise has a rather small contribution to the registration error as compared to the phase difference between the wavefront segments and a larger noise standard deviation might even reduce the impact of phase difference leading to a smaller registration error.

Compared to the plane wavefront the FPR algorithm is slightly less robust to noise concerning the divergent wavefront, which can be explained by the fact that for the divergent wavefront a smaller number of PPO and a larger number of wavefront segments are considered. The less the standard deviation of noise the better the registration performance and results show that for a standard deviation less than 12 nm the FPR algorithm reaches RMS registration errors smaller 10 nm for both wavefronts making the evaluation of high-end optical systems with RMS wavefront errors down to 10 nm possible [26].

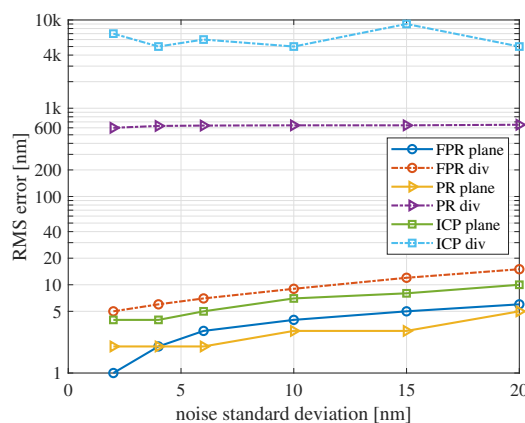


Fig. 10. RMS registration error of the FPR, PR and ICP algorithm for the plane and the divergent wavefront in dependence of the standard deviation of noise.

E. Influence of points per overlap

In the reference configuration all points belonging to the overlap are used for registration, leading to an average number of PPO of 928 for the plane wavefront and 315 for the divergent wavefront. With a larger number of PPO the registration errors might be decreased, as more surface features, crucial for registration, are available and uncertainties, especially those with zero mean, get more compensated. A larger number of PPO, however, increases computation time, as more operations have to be carried out. The computation time and the RMS registration error of the algorithms with respect to the number of PPO used for registration are depicted in Fig. 11. The PPO are uniformly distributed in the overlap area. From the lines in Fig. 11a the computation time of the algorithms in dependence of the PPO is deduced and given

by

$$t_{FPR} = 0.08 + 0.23 \cdot 10^{-3} \text{ PPO},$$

$$t_{PR} = 79 + 0.225 \text{ PPO},$$

$$t_{ICP} = 1.5 + 2 \cdot 10^{-3} \text{ PPO},$$

where $[t] = s$. For all considered numbers of PPO the computation time of the FPR algorithm is between 80 ms and 200 ms and a factor 500 to 2000 smaller than the computation time of the PR algorithm and a factor 10 to 20 smaller than the computation time of the ICP algorithm.

For 100 PPO the RMS registration errors of the FPR algorithm remain smaller than 20 nm considering both wavefronts (see Fig. 11b). For the plane wavefront the PR algorithm is robust with respect to small numbers of PPO and has a RMS registration error smaller 10 nm for 100 PPO. The ICP algorithm shows qualitative registration of the plane wavefront for the maximum number of PPO but has large RMS registration errors up to 100 nm for 300 PPO or less. For the divergent wavefront large variations of the RMS registration error of the PR and ICP algorithm are observed considering different numbers of PPO. This is explained as the PR algorithm gets caught in different local minima, and the ICP algorithm does not reduce phase differences and their impact might change arbitrarily with the number of PPO.

F. Influence of overlap size

Inherently, the registration errors decrease with a larger overlap size, which is explained by multiple reasons. First, the sensibility to out of plane angles between the segments increases. Second, more surface features are available and third more PPO are available. With a larger overlap, however, a larger sensor or more subapertures are necessary increasing measurement time. Moreover, computation time of the algorithm increases if a larger number of PPO or subapertures is considered. In this study the number of subapertures remains constant and while staying at the same position, the subapertures are enlarged to get a larger overlap area and all available PPO are considered for registration.

The registration errors of the algorithms for different overlap sizes are depicted in Table 2. Results show a considerable decrease of the registration errors by 75 % when increasing the overlap size from 20 % to 40 %. In some cases saturation of the improvement is reached and an increase of the overlap size does not lead to a further decrease of registration errors as observed for the FPR and ICP algorithm concerning the divergent wavefront. For the divergent wavefront the step from 30 % to 40 % considerably enlarges the registration errors of the PR algorithm, as it gets caught into a non-optimal local minimum. As all PPO are considered the computation time of the algorithms increases with a larger overlap size. Considering both wavefronts and an overlap size of 40 % the computation time of the FPR algorithm increases from 100 ms to 500 ms, of the PR algorithm from 100 – 200 s to 230 – 330 s and of the ICP algorithm from 2 s to 3.5 s.

In summary the improved registration performance and efficiency of the FPR algorithm is successfully demonstrated and compared to the PR and ICP algorithm, with the algorithm being capable to reconstruct plane and highly divergent wavefronts with RMS registration errors smaller 10 nm. Moreover, the computation time of the proposed algorithm is a factor of up to 20

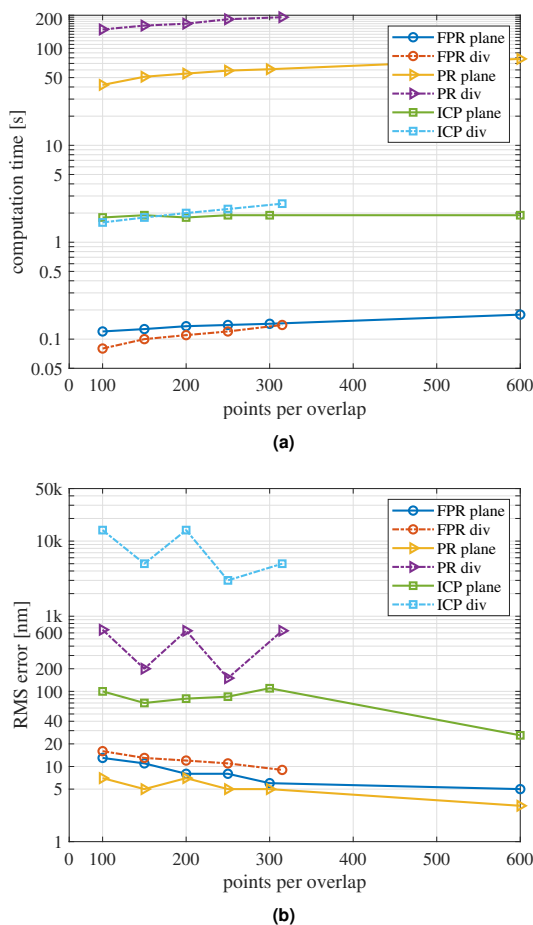


Fig. 11. Computation time (a) and RMS registration error (b) of the FPR, PR and ICP algorithm for the plane and the divergent wavefront in dependence of the average number of points per overlap used for registration.

smaller than the computation time of the ICP algorithm and a factor of up to 1000 smaller than the one of the PR algorithm.

4. CONCLUSIONS

In this paper a fast and precise algorithm for the registration of wavefront segments measured with a scanning SHS setup is presented. It is capable of registering misaligned wavefront segments as well as wavefront segments of different phases, resulting from sensor misalignment or deviations of the scan trajectory from the wavefront of a specific phase. Parallel registration and interpolation of the wavefront segments enables precise reconstruction of the entire wavefront. The registration is carried out by the minimization of a global mismatch metric, which is approximated by a convex function that can be efficiently minimized. In a simulation-based analysis the algorithm is compared with a recently proposed PR algorithm [13] and the point-to-plane ICP algorithm [21]. Sensor misalignment and measurement noise are considered in the analysis and wavefront segments of a plane and a

Table 2. RMS registration error in dependence of overlap size (in % of subaperture area) for FPR, PR and ICP algorithm with respect to the plane and the divergent wavefront.

overlap (%)	FPR plane (nm)	PR plane (nm)	ICP plane (nm)	FPR div. (nm)	PR div. (nm)	ICP div. (nm)
20	4	3	7	9	640	5000
30	2	2	5	11	81	3000
40	1	1	2	4	190	3000

divergent wavefront are registered by the algorithms. While registration performance of the algorithms is comparable for the plane wavefront, the PR and ICP algorithms show large registration errors for the divergent wavefront, as remaining phase differences between the wavefront segments are more critical for this wavefront type. Phase differences between the wavefront segments remain as the PR algorithm gets caught in local minima and the ICP algorithm is incapable of compensating phase differences. The proposed algorithm is flexible with respect to the shape of the wavefront, as the convex function does not contain local but only one global minimum and accurately registers the plane wavefront as well as the divergent wavefront. In particular, for the divergent wavefront the algorithm shows an RMS registration error a factor 75 to 750 smaller than the RMS registration errors of the other algorithms. The FPR algorithm running on a personal computer has a low computation time of about 100 ms for both wavefronts, while the PR algorithm needs about 100 s to 200 s and the ICP algorithm about 2 s. The proposed algorithm registers the wavefronts with high precision, i.e. registration errors smaller 10 nm, enabling real time measurements of high-end optical systems.

Funding. Austrian Federal Ministry for Digital and Economic Affairs; National Foundation for Research, Technology and Development; MICRO-EPSILON MESSTECHNIK GmbH & Co. KG; ATENSOR Engineering and Technology Systems GmbH.

Acknowledgement. We thank Johannes Pfund and Ralf Dorn from Optocraft GmbH for their support and fruitful discussions. The financial support by the Christian Doppler Research Association, the Austrian Federal Ministry for Digital and Economic Affairs, and the National Foundation for Research, Technology and Development, as well as MICRO-EPSILON MESSTECHNIK GmbH & Co. KG and ATENSOR Engineering and Technology Systems GmbH is gratefully acknowledged.

Disclosures. The authors declare no conflicts of interest.

Data availability. Data underlying the results presented in this paper are not publicly available at this time but may be obtained from the authors upon reasonable request.

REFERENCES

1. C. Véraud, M. Le Louarn, V. Korkiakoski, and M. Carillet, "Adaptive optics for high-contrast imaging: pyramid sensor versus spatially filtered Shack—Hartmann sensor," *Mon. Notices Royal Astron. Soc. Lett.* **357**, L26–L30 (2005).

2. J. Liang, B. Grimm, S. Goelz, and J. F. Bille, "Objective measurement of wave aberrations of the human eye with the use of a hartmann–shack wave-front sensor," *JOSA A* **11**, 1949–1957 (1994).
3. D. R. Neal and J. Mansell, "Application of shack-hartmann wavefront sensors to optical system calibration and alignment," in *Adaptive Optics For Industry And Medicine*, (World Scientific, 2000), pp. 234–240.
4. J. Pfund, M. Beyerlein, and R. Dorn, "Shack-hartmann sensors for industrial quality assurance," in *Adaptive Optics for Industry and Medicine*, (Springer, 2005), pp. 141–150.
5. J. Sheldakova, A. Kudryashov, V. Zavalova, and P. Romanov, "Shack-hartmann wavefront sensor versus fizeau interferometer for laser beam measurements," in *Laser Resonators and Beam Control XI*, vol. 7194 (International Society for Optics and Photonics, 2009), p. 71940B.
6. M. Rocktäschel and H. Tiziani, "Limitations of the shack–hartmann sensor for testing optical aspherics," *Opt. & Laser Technol.* **34**, 631–637 (2002).
7. M. E. Fuerst, S. Unger, S. Ito, and G. Schitter, "Wavefront measurement based feedback control for automatic alignment of a high-na optical system," in *Journal of Physics: Conference Series*, vol. 1065 (2018).
8. M. E. Fuerst, E. Csencsics, N. Berlakovich, and G. Schitter, "Automated measurement of highly divergent optical wavefronts with a scanning shack-hartmann sensor," *IEEE Transactions on Instrumentation Meas.* (2020).
9. M. E. Fuerst and G. Schitter, "Scanning wavefront sensor for measurement of highly divergent wavefronts," *IFAC-PapersOnLine*. **52**, 25–30 (2019).
10. D. R. Burada, K. K. Pant, M. Bichra, G. S. Khan, S. Sinzinger, and C. Shakher, "Experimental investigations on characterization of freeform wavefront using shack–hartmann sensor," *Opt. Eng.* **56**, 084107 (2017).
11. R. Schmitt and F. Moenning, "Ensure success with inline-metrology," in *XVIII IMEKO world congress Metrology for a Sustainable Development*, (2006).
12. F. Fang, X. Zhang, A. Weckenmann, G. Zhang, and C. Evans, "Manufacturing and measurement of freeform optics," *CIRP Annals* **62**, 823–846 (2013).
13. N. Berlakovich, M. E. Fuerst, E. Csencsics, and G. Schitter, "Robust wavefront segment registration based on a parallel approach," *Appl. Opt.* **60**, 1578–1586 (2021).
14. D. R. Neal, J. Copland, and D. A. Neal, "Shack-hartmann wavefront sensor precision and accuracy," in *Advanced Characterization Techniques for Optical, Semiconductor, and Data Storage Components*, vol. 4779 (International Society for Optics and Photonics, 2002), pp. 148–160.
15. N. Lindlein, J. Pfund, and J. Schwider, "Expansion of the dynamic range of a shack-hartmann sensor by using astigmatic microlenses," *Opt. Eng.* **39**, 2220–2225 (2000).
16. W. H. Southwell, "Wave-front estimation from wave-front slope measurements," *JOSA*. **70**, 998–1006 (1980).
17. I. Mochi and K. A. Goldberg, "Modal wavefront reconstruction from its gradient," *Appl. Opt.* **54**, 3780–3785 (2015).
18. L. Huang, J. Xue, B. Gao, C. Zuo, and M. Idir, "Zonal wavefront reconstruction in quadrilateral geometry for phase measuring deflectometry," *Appl. optics* **56**, 5139–5144 (2017).
19. S. Rusinkiewicz and M. Levoy, "Efficient variants of the icp algorithm," in *Proceedings third international conference on 3-D digital imaging and modeling*, (IEEE, 2001), pp. 145–152.
20. L. N. Trefethen and D. Bau III, *Numerical linear algebra*, vol. 50 (Siam, 1997).
21. Y. Chen and G. Medioni, "Object modelling by registration of multiple range images," *Image vision computing* **10**, 145–155 (1992).
22. Thorlabs inc., *N-BK7 Positive Meniscus Lens, LE1015-A* (2009).
23. Optocraft GmbH, *SHSCam standard sensor head overview* (2019).
24. L. Huang, J. Xue, B. Gao, C. Zuo, and M. Idir, "Spline based least squares integration for two-dimensional shape or wavefront reconstruction," *Opt. Lasers Eng.* **91**, 221–226 (2017).
25. H. Mao, Y. Liang, J. Liu, and Z. Huang, "A noise error estimation method for shack-hartmann wavefront sensor," in *AOPC 2015: Telescope and Space Optical Instrumentation*, vol. 9678 (International Society for Optics and Photonics, 2015), p. 967811.
26. D. S. Anderson, J. R. P. Angel, J. H. Burge, W. B. Davison, S. T. DeRigne, B. Hille, D. A. Ketelsen, W. C. Kittrell, H. M. Martin, R. H. Nagel *et al.*, "Stressed-lap polishing of 3.5-mf/1.5 and 1.8-mf/1.0 mirrors," in *Advanced optical manufacturing and testing II*, vol. 1531 (International Society for Optics and Photonics, 1992), pp. 260–269.